Chemistry
A European
Journal

Chemistry
Europe
European Chemical
Societies Publishing

Accepted Article

Title: Urchin-type architecture assembled by cobalt phosphide nanorods encapsulated in graphene framework as an advanced anode for alkali metal ion batteries

Authors: Jiamei Wang, Gang Zhu, Zelei Zhang, yi wang, Hui Wang, Jintao Bai, and Gang Wang

To be cited as: *Chem. Eur. J.* 10.1002/chem.202003261

Link to VoR: https://doi.org/10.1002/chem.202003261

WILEY-VCH

Urchin-type architecture assembled by cobalt phosphide nanorods encapsulated in graphene framework as an advanced anode for alkali metal ion batteries

Jiamei Wang,[a,d] Gang Zhu,[c] Zelei Zhang,[a,d] Yi Wang,*[a,d] Hui Wang,[b,d] Jintao Bai,[a,d] and Gang Wang*[a,d]

J. Wang and G. Zhu contributed equally to this work.

[a] J. Wang, Z. Zhang, Dr. Y. Wang, Prof. J. Bai, and Prof. G. Wang
State Key Laboratory of Photoelectric Technology and Functional Materials, International Collaborative Center on Photoelectric Technology and Nano Functional Materials, Institute of Photonics & Photon-Technology
Northwest University
Xi'an 710127, PR China
E-mail: yi.wang@nwu.edu.cn; gangwang@nwu.edu.cn
[b] Prof. H. Wang
Key Laboratory of Synthetic and Natural Functional Molecule Chemistry (Ministry of Education), College of Chemistry & Materials Science
Northwest University
Xi'an 710127, PR China
[c] G. Zhu
School of Chemical Engineering
Xi'an University
Xi'an 710127, PR China
[d] J. Wang, G. Zhu, Z. Zhang, Dr. Y. Wang, Prof. J. Bai, and Prof. G. Wang
Shaanxi Joint Lab of Graphene
Northwest University
Xi'an 710127, PR China

Supporting information for this article is given via a link at the end of the document.

Abstract: Urchin-type cobalt phosphide microparticles assembled by nanorod is encapsulated in graphene framework membrane (CoP@GF), and used as a binder-free electrode for alkali metal ion batteries. Electrochemical measurements indicate that this membrane exhibits enhanced reversible lithium, sodium, and potassium storage capabilities. Moreover, the energy storage properties of CoP@GF electrodes in alkali metal ion batteries display an order of Li > Na > K. DFT calculations on adsorption energy of CoP surfaces for Li, Na, and K indicated that CoP surfaces is more favorable to transfer electrons to Li atoms than Na and K, and the surface reactivity can be ordered as Li-CoP > Na-CoP > K-CoP, thus CoP@GF exhibit better storage capacity for lithium. This work provides experimental and theoretical basis for understand the electrochemical performance of cobalt phosphide-based membrane for alkali metal ion batteries.

Introduction

Rechargeable lithium-ion batteries (LIBs) have been fully exploited and extensively utilized in energy-storage devices such as small electronic vehicles and electrical devices with exceptional performances of excellent reversible capacity and cyclability [1]. With the explosive growth of electric vehicles, there are increasing demands for developing alternative rechargeable battery systems to ease the global resource and energy shortage [2]. Particularly, rechargeable sodium-ion batteries (SIBs) and potassium-ion batteries (KIBs) have been perceived as emerging generations for large-scale stationary applications by virtue of the rich nature abundance of sodium and potassium, and similar energy storage mechanism with LIBs [3-6]. Generally, the performance of these rechargeable alkali metal ion batteries greatly depends on the electrodes. The current commercial electrode material of graphite was unable to fit the requirements of future applications with high energy storage ability owing to its low theoretical capacity and inferior rate capability [7]. Hence, it is of great significance to develop new electrode materials to satisfy the increasing demand of high-performance rechargeable alkali metal ion batteries.

Transition metal phosphides (TMPs) have been regarded as one class of burgeoning anode competitors for rechargeable batteries due to their high theoretical capacities, vivid electrochemical activity, and low operating potentials [8-12]. However, as a kind of conversion-type electrode, most of the TMPs exhibited unsatisfactory energy storage life due to the occurrence of large volume variation during discharge/charge processes [13]. And meanwhile, TMPs usually possess metalloid properties with low electrical conductivity, which unavoidably hinders the mobility of electrons, resulting in inferior rate performance. To track the above issues, the construction of hybrid structure materials consisted of TMPs and carbonaceous materials have been confirmed as an efficient approach [14-16]. On account of the excellent mechanical property and high conductivity of carbonaceous materials, the combination of TMPs with them can not only accommodate the volume effect, but also enhance electrochemical kinetics of TMPs by increasing the electron conductivity [17-19]. In addition, the carbonaceous materials often possess large specific surface areas, which can prevent the TMPs particles from aggregation by acting as dispersed matrices to increase active sites for highly efficient energy storage.

For the preparation of hybrid electrodes in rechargeable alkali metal ion battery systems, the traditional processes involve coating slurry consisting of an active material, a conductive reagent, and a binder onto a metal current collector [20-22]. The used binders are electrochemical inactive materials. The addition of them in the conventional hybrid electrodes is indispensable but provides little capacity and occupies the electrode weight unavoidably. Furthermore, the used binders are generally composed of insulated fluorine-based polymeric compounds. The existence of them will increase the electrode resistance. In view of the shortcomings provided by the binders, the practical energy storage properties of the conventional hybrid electrodes are more or less unsatisfactory. Hence, it is highly essential to fabricate electrodes without binders to realize enhanced electrochemical properties and robust mechanical flexibility. Binder-free membrane electrodes thus have stood out over the years [23-26]. The electrodes can completely eliminate the introduction of binders, realize stable electrical contact with conductive matrix, accelerate ion transmission, and improve the gravimetric energy storage capacity of batteries. In view of the advantages for the electrodes, construct carbon-modified TMP hybrid into binder-free membrane to realize flexible electrodes with high performance has been becoming critically important. Nevertheless, the studies of the binder-free carbon-modified TMP are quite lacking. Furthermore, it should be remarkable that the current studies mainly focused their interests on the lithium storage performance of TMPs, the sodium and potassium storage properties of TMPs gained insufficient attention. Therefore, it is necessary and significative to develop binder-free TMP-based membrane electrodes that can be used in alkali metal ion batteries with high performance.

On the basis of the above research situations for TMP electrodes, herein, we described a simple strategy to fabricate urchin-type cobalt phosphide encapsulated in graphene framework (CoP@GF) hybrid membrane as an intriguing binder-free electrode for alkali metal ion batteries. The strategy for the fabrication of the electrode involved the synthesis of CoP microspheres by hydrothermal approach, assembly of the CoP with graphene oxide to form CoP@graphene oxide hybrid membrane by vacuum filtration, and subsequent conversion into CoP@GF hybrid membrane through thermal treatment (Fig. S1). The fabricated membrane electrode consisted of high-conductivity GF as flexible substrate and conductive matrix, and urchin-type CoP as active material. This study shed light on the use of CoP-based membrane as a binder-free electrode that can be worked efficiently for high performance alkali metal ion battery systems. In addition, our electrochemical results indicated that the energy storage properties of CoP@GF electrode in alkali metal ion batteries with an order of LIBs > SIBs > PIBs. The adsorption energy of CoP surfaces for the Li, Na, and K was studied through density functional theory (DFT) method to clarify the phenomenon. The result may provide theoretical basis for further understand the electrochemical property of CoP-based membrane for alkali metal ion batteries.

Results and Discussion

The crystal structures of the obtained products were confirmed by XRD measurements. The well-defined peaks in the XRD pattern can be ascribed to $Co(CO_3)0.5(OH)\cdot0.11H_2O$ (JCPDS No. 48-0083) (Fig. S2). After a phosphatization process, $Co(CO_3)0.5(OH)\cdot0.11H_2O$ was turned into CoP. XRD result in Fig. 1a demonstrates fifteen peaks at 23.6°, 31.6°, 32.0°, 35.3°, 36.3°, 36.6°, 38.9°, 45.1°, 46.2°, 48.1°, 48.4°, 52.2°, 56.0°, 56.3° and 56.7°, corresponding to (101), (011), (002), (200), (111), (102), (201), (210), (112), (211), (202), (103), (020), (212), and (301) of CoP with orthorhombic phase (JCPDS No. 29-0497), respectively. The corresponding crystal structure of CoP is exhibited in Fig. 1b. In addition, the sample of CoP@GF membrane and CoP have similar XRD pattern. It is remarkable that the peak at 25° in CoP@GF membrane corresponds to GF.

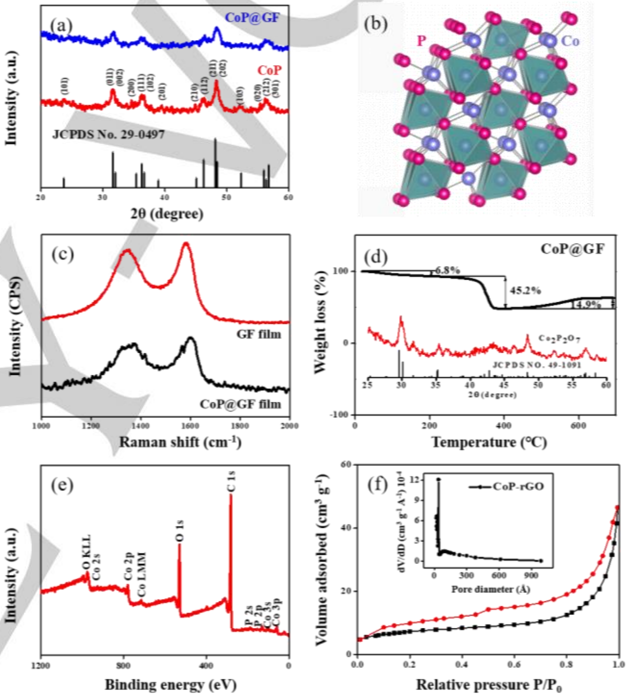

Figure 1. XRD patterns of CoP@GF membrane and CoP (a), crystal structure of orthorhombic CoP (b), Raman spectra of CoP@GF hybrid membrane and GF membrane (c), TGA curve of the CoP@GF hybrid membrane (d, inset presents the XRD pattern of the residue after the TGA test), Full XPS spectrum of the CoP@GF hybrid membrane (e), N_2 adsorption-desorption isotherm curves of CoP@GF (f, inset presents their pore size distributions).

The carbon structure information of the obtained products was explored by Raman spectroscopy. As displayed in Fig. 1c, both of the two samples show two prominent peaks at ~1355 and 1580 cm^{-1}, which can be ascribed to the D and G band, respectively [27]. And the I_D/I_G intensity ratio reflects the disorder degree or defects for carbon structure. Detailed analysis shows that the intensity ratios of the D band to G band (I_D/I_G) is 0.9 for GF membrane, a little lower than that of CoP@GF membrane (0.96), indicating more defects/disorders have been introduced after the introduction of CoP into GF and thus more active sites will be provided during the cyclic process.

The mass fraction of CoP in the CoP@GF membrane was calculated by TGA investigation. As exhibited in Fig. 1d, the little weight loss of 6.8% can be ascribed to the weight of water, which was absorbed from the air [28]. After that, the TGA curve of CoP@GF membrane shows a major weight loss between 300 and 400 ^oC, which can be assigned to the combustion of carbon and gradual oxidation of CoP to Co_3O_4 and P_2O_5 [29,30]. On further increasing the temperature, a subsequent increase in weight can be observed between 400-620 ^oC, which can be ascribed to the formation of the complete oxidation product of $Co_2P_2O_7$ on the basis of the XRD analysis of the residue after the TGA test (Fig. 1d) [31]. This result indicates the CoP in the membrane was converted into $Co_2P_2O_7$ at the temperature of higher than 400 ^oC in air atmosphere. Accordingly, the CoP content in the membrane is calculated to be 49.5%.

XPS measurements were performed to examine the chemical states of the CoP@GF membrane. The XPS survey spectrum indicates that the CoP@GF membrane consists of P, Co, O and C elements (Fig. 1e). The chemical states of P, C, and Co were identified by the high-resolution spectra of P 2p, Co 2p and C 1s, respectively (Fig. S3a-c). The Co 2p spectrum (Fig. S3a) can be decomposed into five peaks at 781.8, 797.5, 785.6, 787.5 and 803.1 eV. The former two peaks are corresponded to the Co $2p_{3/2}$ and Co $2p_{1/2}$, respectively, while the other peaks are consistent with satellite bands [32]. The high-resolution P 2p spectrum for the CoP@GF membrane (Fig. S3b) is split to three peaks at 129.7, 130.7, and 133.8 eV. The former two peaks are corresponded to the P $2p_{2/3}$ and P $2p_{1/2}$ of P-Co bond, respectively, while the last one is consistent with P-O bond [33]. The high-resolution C 1s spectrum for the CoP@GF membrane (Fig. S3c) can be factored into the main peak at 284.2 eV indexed to C-C/C=C and two minor peak located at 286.1 and 287.8 eV, which are assigned to C-O and O-C=O bonds, respectively [34].

The N_2 adsorption/desorption tests were executed to further estimate the porosity properties and the surface areas of the CoP and CoP@GF. As displayed in Fig. 1f and Fig. S3d, the specific surface area of CoP@GF was calculated to be 23.1 m^2 g^{-1}, which was larger than CoP (15.3 m^2 g^{-1}). The increased specific surface area of CoP@GF may be attributed to the introduction of GF, which is beneficial to enhance the metal ion surface interactions through expanding the quantity of exposed active sites [35]. The pore size distribution (inset) also verifies that the porous structure consisting chiefly of mesoporous. The mesoporous intrinsic quality accommodates the volume changes during cycling, as well as facilitate the electrical conductivity by provides a good electron pathway [36]. In addition, the type-IV N_2 sorption isotherms further demonstrate the mesoporous feature of two samples.

The morphology of CoP was assessed by SEM, TEM and high-resolution TEM (HRTEM). The SEM images (Fig. 2a-b) reveal hierarchical urchin-type CoP spheres have an average diameter of 15-20 µm, and each sphere is assembled from nanorods as building blocks. In addition, there are many cavities among the nanorods, which provide more active sites and ensure excellent electrolyte workability during the redox reaction. The detailed structure of CoP microparticles was characterized by TEM and HRTEM. The TEM images (Fig. 2c and d) reveal that the CoP has urchin-type structure and with the size about 15 µm, which is in accord with the SEM result. The TEM element mapping images in Fig. 2e indicate the homogeneous dispersion of Co and P in the urchin-type structure. TEM image on a single CoP nanorod suggests the building blocks of the CoP have an average radius about 80 nm (Fig. 2f). The HRTEM image and Fast Fourier Transform (FFT) pattern of CoP is shown in Fig. 2g. The lattice distances are determined to be 0.28 and 0.25 nm, which was in line with the (011) and (111) crystal planes of CoP, respectively. The morphology of GF membrane was also characterized by SEM. Fig. S4a-b show the surface of the GF membrane, indicating that the GF flakes connected to each other and formed a frizzy surface. The cross-sectional SEM images of GF membrane in Fig. S4c and d demonstrate the thickness of layered GF membrane was 10.2 µm.

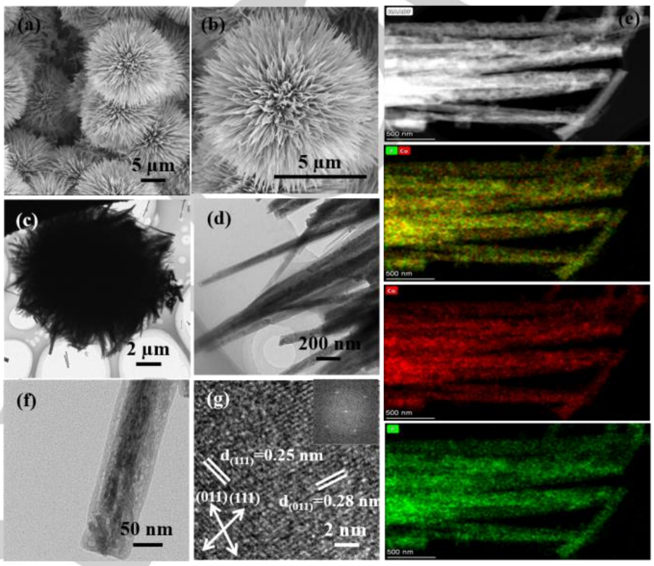

Figure 2. SEM images of urchin-type CoP (a & b), TEM images of urchin-type CoP (c & d), TEM element mapping images for CoP (e), TEM image on a single CoP nanorod (f), HRTEM image of CoP (g, inset presents its FFT pattern)

In order to study the influence of CoP on the morphology and structure of GF membrane, the CoP@GF membrane was also measured by SEM measurement (Fig. 3). The surface SEM images of the CoP@GF membrane (Fig. 3a-d) reveal that the CoP with the range of 10-25 µm are uniformly distributed in the 3D interconnected GF framework and GF maintain a 3D continuous network structure without any fracture. The cross-sectional morphology of CoP@GF membrane (Fig. 3c-d) reveals that the layer thickness of the membrane has changed from 10.2 to 25.6 µm. In addition, the number of CoP intersperse uniformly into the GF membrane to forming a continuous conductive network with a sandwiched architecture. This unique membrane electrode possesses excellent mechanical flexibility (Fig. S5) and can completely eliminate the introduction of binders, realize sturdy electrical contact with conductive matrix, accelerate ion transmission, and improve the gravimetric energy storage capacity of batteries. In addition, the surface characteristic of the CoP@GF membrane, GF membrane and CoP were also evaluated by the contact angle measurements. As shown in Fig. S6, when a water droplet drops on the surface of CoP, it quickly seeps into the material, indicating the hydrophilic of CoP. However, when a drop of water falls on the CoP@GF membrane, it is repelled by the hydrophobicity of graphene, and thus exhibits the large contact angle of 103^o, even after 10 s, the water droplet still keeps the contact angle of 98^o. This

10.1002/chem.202003261

hydrophobic property is conducive to organic electrolyte transport.

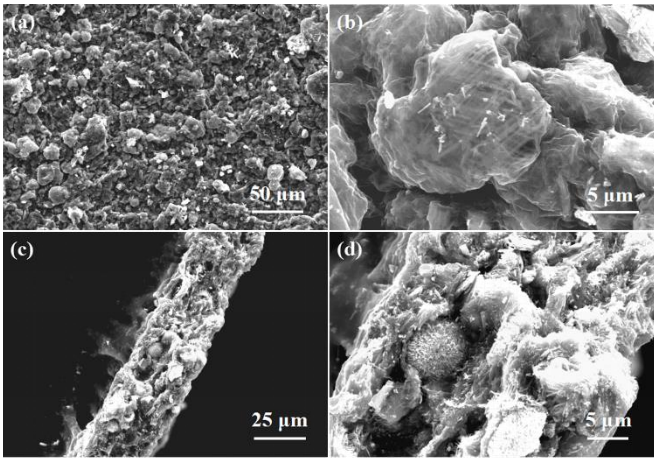

Figure 3. Surface SEM images of CoP@GF membrane (a & b), cross-sectional SEM images of CoP@GF membrane (c & d).

The electrochemical property of the CoP@GF membrane for LIBs was compared with urchin-type CoP. The cyclic voltammetry (CV) curves were measured in the potential range of 0-3 V vs. Li/Li$^+$ at 0.1 mV s^{-1}. As depicted in Fig. 5a and Fig. S7a, CoP@GF membrane and CoP anodes show similar peaks, revealing that they experienced similar redox reaction process. During the cathodic Li$^+$ insertion process at the initial cycle, a wide peak at 1.12 V is consistent with the form of lithium intercalation into the CoP and a solid electrolyte interface (SEI) film. During the anodic Li$^+$ extraction process of the initial cycle, the oxidation peaks at 1.08 V could be related to the lithium-extraction reaction [29]. In the subsequent cycles, the previous cathodic peak location shifts to 0.6 V, which can be contributed to the structural rebuilding during the activation process, while the position of anodic peak is basically unchanged, demonstrating the reversibility of redox reaction during the anodic lithium extraction process. Compared to the CoP, the CV curves of CoP@GF membrane overlapped well with each other during the 2nd and 3rd cycle, implying the excellent cyclability and reversibility of the CoP@GF electrode.

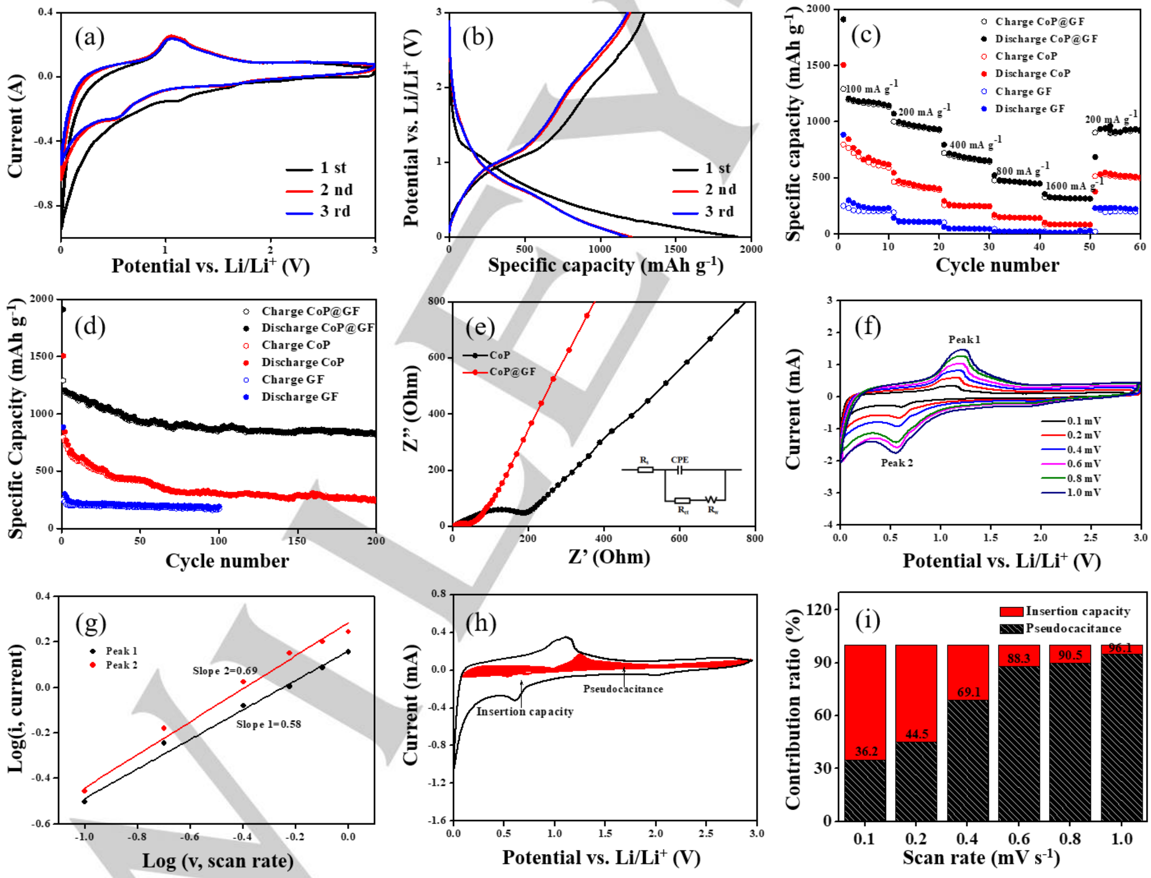

Figure 4. Electrochemical behaviors for Lithium storage: (a) CV curves of CoP@GF membrane at 0.1 mV s^{-1}, (b) discharge and charge curves for CoP@GF membrane at 100 mA g^{-1}, (c) comparison of rate properties of the CoP@GF membrane, CoP powder and GF membrane electrodes, (d) comparison of cycle capabilities of the CoP@GF membrane, CoP powder and GF membrane electrodes, (e) Nyquist plots of the CoP@GF membrane and CoP powder, (f) CV profiles of CoP@GF membrane at different scan rates, (g) the fitted lines and log (peak current) versus log (sweep rate), (h) capacitive contribution (red area) at a scan rate of at 0.1 mV s^{-1}, and (i) percentage capacitive contributions at different scan rates of CoP@GF membrane.

The galvanostatic profiles of CoP@GF membrane and CoP anodes at 100 mA g^{-1} are presented in Fig. 4b and Fig. S7b, respectively. During the first cycle, CoP and CoP@GF membrane anodes show the similar voltages of the discharge and charge plateaus. In the first discharge process, an obvious stable slope between 1.0~1.2 V, followed by a slowly reduce to 0 V. In the 2nd and 3rd discharge cycle, a slope emerged between 0.8~0.6 V. In the charging process, a slope appeared between 0.9~1.2 V. This result identifies with the CV measurement. The initial discharge capacities of CoP and CoP@GF membrane are 1501 and 1881 mAh g^{-1}, respectively. And the corresponding initial charge capacities are 785 and 1281 mAh g^{-1}, which indicates that the initial coulombic efficiency of CoP@GF membrane is higher than the CoP. In the subsequent two cycles, the voltage platform of CoP@GF membrane almost overlapped, implying a better cyclability and reversibility of the membrane.

Rate performances of GF, CoP and CoP@GF membrane electrodes were exhibited and compared at varied currents raised from 100 to 1600 mA g^{-1} (Fig. 4c). The CoP@GF membrane exhibits the best rate performance with reversible capacities of 1120, 901, 632, 415, and 283 mAh g^{-1} at 100, 200, 400, 800 and 1600 mA g^{-1}, respectively. While the CoP anode exhibits a poor rate capability with reversible capacities of 601, 407, 228, 143, and 73 mAh g^{-1} at the similar measure conditions. GF membrane anode exhibits the worst rate behavior most likely due to its own limited theoretical capacity. When the current back to 100 mA g^{-1}, the capacity of CoP@GF membrane anodes reaches 880 mAh g^{-1}, which is on the verge of the capacity of its first lap. As for CoP, only 284 mAh g^{-1} was acquired at the similar currents. All of the above results illustrate that the CoP@GF membrane possesses a highest rate capacity among these three anodes.

The cycling stability of GF, CoP and CoP@GF membrane electrodes at 100 mA g^{-1} were exhibited and compared in Fig. 4d. It is clearly observed that the CoP@GF membrane and GF membrane electrodes reveal more stable cycling performances than the CoP electrode. And the CoP@GF membrane exhibits a large capacity of 832 mAh g^{-1} after 200 cycles due to its unique sandwich structure. However, the CoP decays rapidly from 1508 to 219 mAh g^{-1}. The GF membrane maintains a stable trend but only has a capacity of 172 mAh g^{-1} after 100 cycles. The rapid capacity decay of CoP is attributed to the “dead surface” caused by traditional polymer adhesive. Table S1 presents the electrochemical performance comparison of the CoP@GF membrane electrode and other cobalt phosphide-C anodes for LIBs. The lithium storage performance of the CoP@GF membrane is better than those of other reported counterparts. The long cycle life of the membrane electrode was further evaluated at a current density of 1000 mA g^{-1} (Fig. S8). The membrane delivers a reversible capacity of 260 mAh g^{-1} after 420 cycles with the capacity retention of 88% of the 2nd cycle capacity.

Fig. 4e displays the impedance spectra of the CoP@GF membrane and CoP electrodes. Apparently, all the plots are made up of a straight line at the low frequency region and a depressed semicircle at the high frequency region. The simulated equivalent circuit includes ohmic resistance of the electrolyte (R_s), the charge-transfer resistance (R_{ct}), Warburg impedance (R_w), constant-phase element (CPE). The simulation results in Table 1 show that the value of R_s for CoP@GF is much lower than that of CoP. And the R_{ct} of CoP@GF membrane (45.4 Ω) is lower than that of CoP powder (169.4 Ω), suggesting the faster charge transport kinetics of CoP@GF membrane. Moreover, The EIS was also used to calculate the diffusion coefficient of Li^+ (D). The σ values were obtained from the linear fitting in Fig. S9 to be 79.1 for CoP@GF membrane and 507.3 for CoP powder, and the lithium diffusion coefficient of CoP@GF membrane and CoP can be acquired to be about 4.6×10^{-8} and 1.1×10^{-9} cm^2 S^{-1}, respectively. It can be found from the result that the avoidance usage of adhesives can greatly reduce the internal resistance of the battery. In addition, the carbon skeleton conductive structure leads to remarkably fast electronic transfer channels for enhanced electrochemical property, which could be also another key factor to decrease the resistance of CoP@GF membrane electrode.

Table 1. Simulated values of EIS for CoP and CoP@GF electrodes in the LIB system.

Sample	R_s (Ohm)	R_{ct} (Ohm)	σ (Ω $s^{-1/2}$)	D_{Li} (cm^2 S^{-1})
CoP	9.3	169.4	507.3	1.1×10^{-9}
CoP@GF	2.3	45.4	79.1	4.6×10^{-8}

The reaction kinetics of the CoP@GF membrane anode was further analyzed by CV tests with sweep rates from 0.1 to 1.0 mV s^{-1}. As displayed in Fig. 4f, with the sweep rate increased, the pair of redox peaks of the CoP@GF membrane anode deviates from the initial position bit by bit owing to ohmic resistance. As seen in Fig. 4g, the b-values of CoP@GF membrane for peak 1 and 2 are 0.58 and 0.69 respectively. It illustrates the diffusion-controlled conversion reaction and pseudocapacitive behavior both occurred in the redox process. As presented in Fig. 4h, the pseudocapacitive contribution of CoP@GF membrane electrodes is 36.2% obtained at 0.1 mV s^{-1}. As presented in Fig. 4i, the contribution of pseudocapacitive for the CoP@GF membrane electrode are 36.2, 44.5, 69.1, 88.3, 90.5, and 96.1% at the sweep rates of 0.1, 0.2, 0.4, 0.6, 0.8, and 1.0 mV s^{-1}, respectively. The result demonstrates that the percentage capacitive contributions are increasing as the increasing of sweeps, signifying that the pseudocapacitive behavior is the mechanism for CoP@GF membrane to exhibit high rate property.

The electrochemical properties of the CoP@GF membrane for use in SIBs were also investigated and compared with those of urchin-type CoP in this work. The CV curves were measured in the potential range of 0-3 V vs. Na^+/Na under a scan rate of 0.1 mV s^{-1}. As shown in Fig. 5a and Fig. S10a, CoP@GF membrane and CoP anodes show similar peaks, revealing that they experienced similar sodiation/desodiation process. In the first cathodic process, a wide peak at about 1.0-0.0 V is consistent with the sodium ion intercalation into the CoP and the formation of the SEI membrane. In the first anodic process, the peaks at 1.5 and 1.9 V can be attributed to the multistep desodiation of Na_3P [37]. In the following cathodic processes, the previous cathodic peak location shifts to 1.3 V, which can be contributed to the structural rebuilding in the activation process. Compared to the CoP, the CV curves of CoP@GF membrane overlapped well with each other during the 2nd and 3rd cycle, demonstrating the good energy-storage reversibility of the electrode. Fig. 5b and Fig. S10b show the discharge/charge curves of the CoP and the CoP@GF membrane at a current of 50 mA g^{-1}. In the first cycle, CoP and CoP@GF membrane anodes exhibit the similar discharge/charge potential platform. In the initial discharge procedure, an obvious stable slope between 1.0~0.5 V, followed by a slowly reduce to 0 V. After it, a slope emerged between 1.5~1.2 V. In the charging procedure, a slope appeared between 0.5~2.0 V. This result is in accordance with the CV profiles. The discharge capacities of CoP and the CoP@GF for the first cycle were 384 and 554 mAh g^{-1}, respectively. And the corresponding charge capacities for the first cycle were 267 and 438 mAh g^{-1}, which signify that the initial coulombic efficiency of CoP@GF is higher than CoP. During the 2nd and 3rd cycle, the discharge/charge curves of CoP@GF almost overlapped, revealing a stable cycling capability of CoP@GF membrane.

The rate capabilities of GF, CoP and CoP@GF membrane anodes at different rates from 50-800 mA g^{-1} were also measured (Fig. 5c). Among them, the CoP@GF membrane anodes exhibits the good rate performance with the best reversible capacities at various rates, and it can deliver a reversible capacity of 368, 299, 223, and 164 mAh g^{-1} at 50, 100, 200 and 400 mA g^{-1}, respectively. Even at the high rate of 800 mA g^{-1}, the reversible capacity of 101 mAh g^{-1} can still be acquired. While the CoP anode exhibits the lesser rate performance with reversible capacities of 222, 173, 129, 94, and 54 mAh g^{-1} at the identical test conditions. GF membrane anode exhibits the worst rate behavior most likely due to its own limited theoretical capacity. When the current rate is returned to 50 mA g^{-1}, the capacity of CoP@GF membrane anodes reaches 341 mAh g^{-1}, which is close to the capacity of its first lap. As for CoP, only 189 mAh g^{-1} was obtained. All of these results demonstrate that the superb rate capability of CoP@GF membrane anode. Fig. 5d compares the cycling stability of GF, CoP and CoP@GF membrane anodes at 50 mA g^{-1}. It is clearly observed that CoP@GF membrane delivers the best cycling stability. The CoP@GF membrane maintains a discharge capacity of 305 mAh g^{-1} after 200 cycles, which is much better than the 191 mAh g^{-1} for CoP and 89 mAh g^{-1} for GF membrane after 70 cycles. The sodium storage performance of the membrane with microscale CoP is highly competitive compared to other cobalt phosphid-C electrode materials with nanoscale (Table S2). To evaluate the long-term cycling performance of the membrane electrode, the CoP@GF is further cycled at 400 mA g^{-1} (Fig. S11). After 280 cycles, the reversible capacity remained at 132 mAh g^{-1}, corresponding to the capacity retention of 80% relative to the capacity at the 2nd cycle.

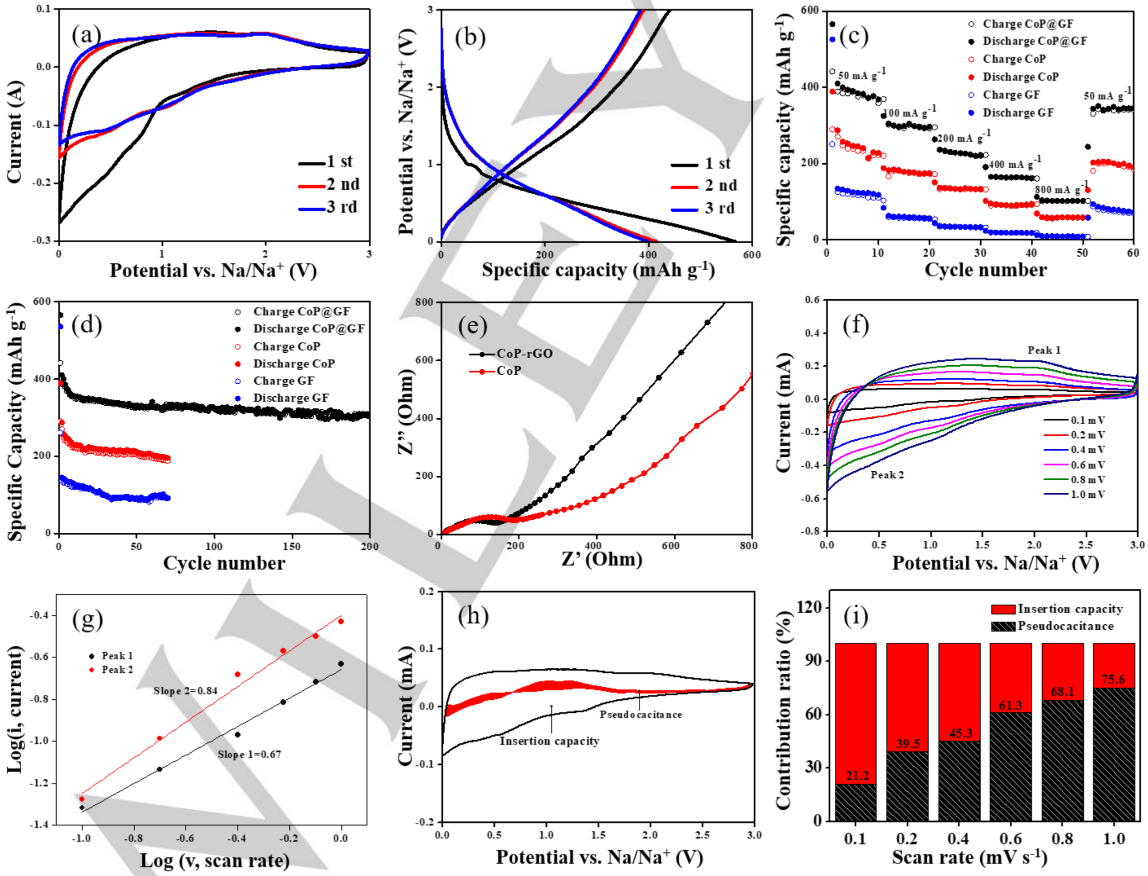

Figure 5. Electrochemical behaviors for sodium storage: (a) CV curves of CoP@GF membrane at 0.1 mV s^{-1}, (b) discharge and charge curves for CoP@GF membrane at 100 mA g^{-1}, (c) comparison of rate properties of the CoP@GF membrane, CoP powder and GF membrane electrodes, (d) comparison of cycle capabilities of the CoP@GF membrane, CoP powder and GF membrane electrodes, (e) Nyquist plots of the CoP@GF membrane and CoP powder, (f) CV profiles of CoP@GF membrane at different scan rates, (g) the fitted lines and log (peak current) versus log (sweep rate), (h) capacitive contribution (red area) at a scan rate of at 0.1 mV s^{-1}, (i) percentage capacitive contributions at different scan rates of CoP@GF membrane.

Table 2. Simulated values of EIS for CoP and CoP@GF electrodes in the SIB system.

Sample	R_s (Ohm)	R_{ct} (Ohm)	σ (Ω $s^{-1/2}$)	D_{Na} (cm^2 S^{-1})
CoP	10.5	162	622.1	0.7×10^{-9}
CoP@GF	9.3	121.4	450.3	1.3×10^{-9}

Nyquist plots of the CoP@GF and CoP electrodes are displayed in Fig. 5e in the SIB system. The simplified equivalent circuit diagram of impedance spectra is the same as LIBs. The simulation results in Table 2 shows that the value of R_s for CoP@GF anode is nearly equal to CoP anode, implying two cells were assembled and measured under the same conditions. Additionally, a much better sodium ion transmission coefficient was found on CoP@GF electrode (1.3×10^{-9} cm^2 S^{-1} for CoP@GF, and 0.7×10^{-9} cm^2 S^{-1} for CoP), suggesting the faster charge transport kinetics of CoP@GF membrane (Fig. S12).

The sodium storage kinetic of the CoP@GF membrane electrode was further analyzed by CV tests with sweep rates ranged from 0.1 to 1.0 mV s^{-1}. The analysis and the calculation method in the SIB system are similar to that in LIB system. As shown in Fig. 5f, peak currents for CoP@GF membrane electrode increased as the sweep rates raised. As seen in Fig. 5g, the b-values CoP@GF membrane for peak 1 and 2 are 0.84 and 0.67, respectively. It illustrates that the diffusion-controlled conversion reaction and pseudocapacitive behavior both occurred in the redox process. As depicted in Fig. 5h, the pseudocapacitive contribution of CoP@GF membrane electrodes is 21.2% obtained at 0.1 mV s^{-1}. As presented in Fig. 5i, the pseudocapacitive contribution of the CoP@GF membrane electrode are 21.2, 39.5, 45.3, 61.3, 68.1, and 75.6% at the sweep rates of 0.1, 0.2, 0.4, 0.6, 0.8, and 1.0 mV s^{-1}, respectively. The result demonstrates that the contribution ratio of the pseudocapacitance is augmented with increasing of sweep, signifying that the pseudocapacitive behavior is the mechanism for CoP@GF membrane to exhibit high rate capability.

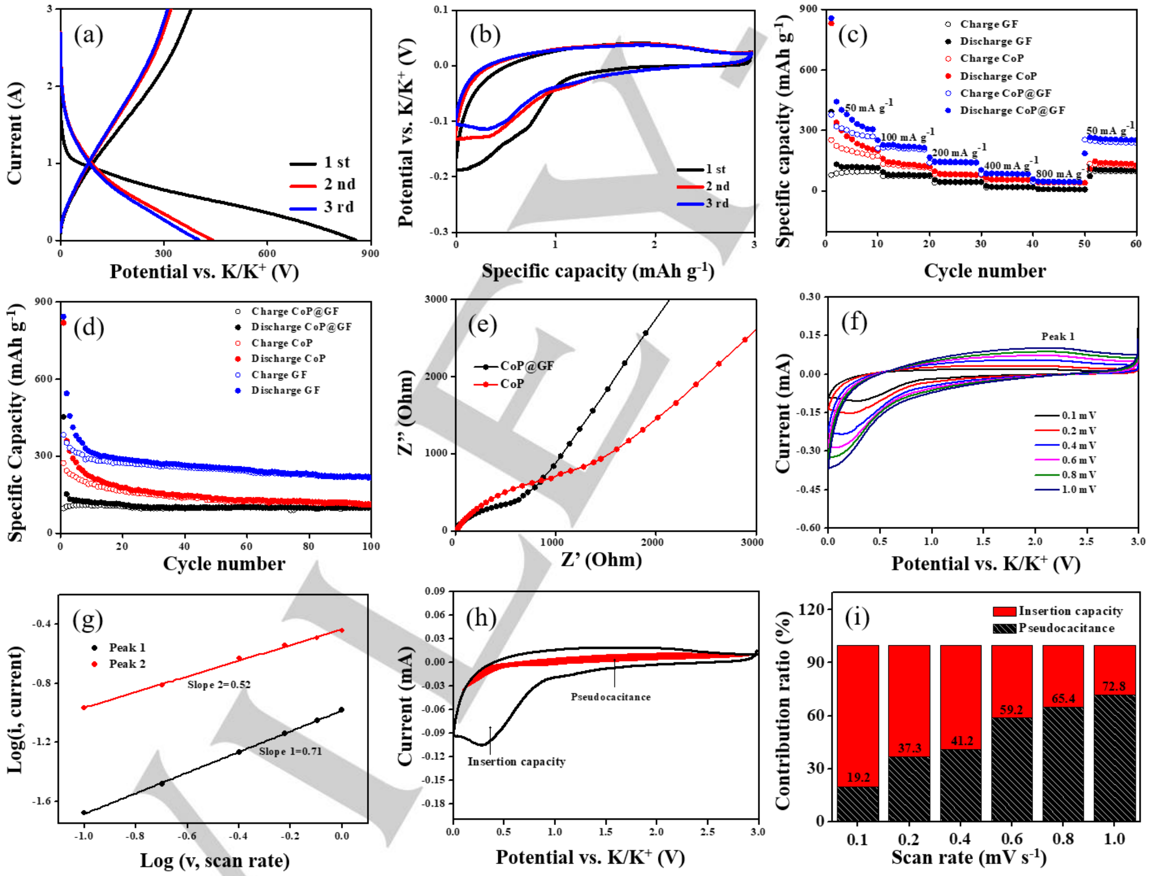

Figure 6. Electrochemical behaviors for potassium storage: (a) CV curves of CoP@GF membrane at 0.1 mV s-1, (b) discharge and charge curves for CoP@GF membrane at 100 mA g-1, (c) comparison of rate properties of the CoP@GF membrane, CoP powder and GF membrane electrodes, (d) comparison of cycle capabilities of the CoP@GF membrane, CoP powder and GF membrane electrodes, (e) Nyquist plots and of the CoP@GF membrane and CoP powder, (f) CV profiles of CoP@GF membrane at different scan rates, (g) the fitted lines and log (peak current) versus log (sweep rate), (h) capacitive contribution (red area) at a scan rate of at 0.1 mV s^{-1}, (i) percentage capacitive contributions at different scan rates of CoP@GF membrane.

Considering the excellent lithium and sodium storage capabilities of the CoP@GF membrane, its electrochemical properties for PIBs were further investigated. The electrochemical reactions were obtained by CV tests at 0.1 mV s^{-1} with the potential range of 0-3 V vs. K^+/K. As displayed in Fig. 6a and Fig. S13a, CoP@GF membrane and CoP anodes exhibit similar CV profile evolution, revealing that the two electrodes had experienced similar redox reaction process. In the initial cathodic procedure, a wide peak at about 1.0-0.0 V is consistent with the potassium ion intercalation into the CoP and the formation of the SEI membrane. In the followed discharge processes, a couple of cathodic peaks at 0.5/1.1 V can be found, which is ascribed to the potassiation/depotassiation [38]. While the positions of anodic peak is basically unchanged, demonstrating the reversibility of redox reaction during the anodic potassiation process. Compared to the CoP, the CV curves of CoP@GF membrane were overlapped after the 2nd cycle, demonstrating the excellent energy-storage reversibility. Fig. 6b and Fig. S13b show discharge/charge curves of the CoP and the CoP@GF membrane at a current of 50 mA g^{-1}. In the first cycle, CoP and CoP@GF membrane anodes show the similar discharge/charge potential platform. In the first discharge cycle, an obvious stable slope between 1.0~0.0 V can be found. In the following discharge cycles, a slope emerged between 1.5~1.2 V. In the charging process, a slope appeared between 0.5~2.0 V. This results in accordance with the above CV results. The initial coulomb efficiencies of CoP and the CoP@GF were 45 and 34%, respectively, which signify that both CoP and CoP@GF electrodes have a low initial coulombic efficiency. The low initial coulombic efficiencies could be the result of the irreversible generation of the SEI membrane. During the following cycles, the discharge/charge profiles of CoP@GF almost overlapped, revealing a stable cycling capability of the CoP@GF membrane.

The rate properties of GF, CoP and CoP@GF membrane anodes for PIB at different rates from 50-800 mA g^{-1} were also measured (Fig. 6c). In general, the CoP@GF membrane anodes exhibits the good rate performance with the best reversible capacities at various rates, and it can deliver a reversible capacity of 305, 213, 140, 85, and 38 mAh g^{-1} at 50, 100, 200, 400, and 800 mA g^{-1}, respectively. By contrast, the rate performance of CoP anode is slightly inferior to sandwich-shaped CoP@GF electrode with reversible capacities of 192, 121, 83, 59, and 32 mAh g^{-1} at the identical test conditions. GF membrane anode exhibits the worst rate behavior most likely due to its own limited theoretical capacity. When the current rate returned to 50 mA g^{-1}, the capacity of CoP@GF membrane anode attains 251 mAh g^{-1}, which is the capacity of its first cycle. As for CoP, only 127 mAh g^{-1} was obtained. These comparison results demonstrate the superb rate respons of the CoP@GF membrane anode. Fig. 6d compares the cycling stability of GF, CoP and CoP@GF membrane anodes at 50 mA g^{-1}. It is clearly observed that CoP@GF membrane shows the highest cycling stability with the discharge capacity of 216 mAh g^{-1} after 100 cycles, which is much higher than the CoP (104 mAh g^{-1}) and GF membrane (89 mAh g^{-1}) after 100 cycles. The cycling performance of CoP@GF membrane in this work compares favorably with those of the previously reported cobalt phosphide-C nanomaterials for PIBs (Table S3). Moreover, when cycled at 400 mA g^{-1}, the membrane electrode exhibits a reversible capacity of 62 mAh g^{-1} after 250 cycles with 60% capacity retention of the 2nd cycle capacity (Fig. S14). Comparatively speaking, the potassium storage performance of the membrane is inferior to its lithium and sodium storage properties, which may be attributed to the larger radius of K^+ (0.136 nm) compared to Li^+ (0.076 nm) and Na^+ (0.102 nm), resulting in relatively worse reaction kinetics during cycling [39,40].

Nyquist plots of the CoP@GF and CoP electrodes are displayed in Fig. 6e in the PIB system. The simulation results in Table 3 shows that the value of Rs for CoP@GF anode is nearly equal to CoP anode, implying two electrodes cells were assembled and measured under the same conditions. Moreover, a larger potassium ion diffusion coefficient was observed on CoP@GF electrode (5.5×10^{-10} cm^2 S^{-1} for CoP@GF, and 1.5×10^{-10} cm^2 S^{-1} for CoP), suggesting the faster charge transport kinetics of CoP@GF membrane (Fig. S15). The enhanced electron transfer, kinetics of ion diffusion could be the major reason for the improved potassium storage property of CoP@GF membrane.

Table 3. Simulated values of EIS for CoP and CoP@GF electrodes in the PIB system.

Sample	R_s (Ohm)	R_{ct} (Ohm)	σ (Ω $s^{-1/2}$)	D_K (cm^2 S^{-1})
CoP	5.9	952.8	1337.6	1.5×10^{-10}
CoP@GF	5.1	617.8	715.4	5.5×10^{-10}

To provide deep insight into the potassium storage kinetic of the CoP@GF membrane, the electrode was further analyzed by CV tests with scan rates from 0.1-1.0 mV s^{-1} (Fig. 6f). As depicted in Fig. 6g, the b-values of CoP@GF membrane for peak 1 and 2 are 0.52 and 0.71 respectively. It illustrates that the diffusion-controlled conversion reaction and pseudocapacitive behavior both occurred in the potassiation/depotassiation process. As presented in Fig. 6h and i, the capacitive contribution of the CoP@GF membrane anode are 19.2, 37.3, 41.2, 59.2, 65.4 and 72.8% at the sweep rates of 0.1, 0.2, 0.4, 0.6, 0.8 and 1.0 mV s^{-1}, respectively. The result demonstrates that the percentage capacitive contribution is increasing as the increasing of sweep, signifying that the pseudocapacitive behavior is the mechanism for CoP@GF membrane to exhibit high rate capability. It is noteworthy that capacitive contribution for PIB system lower than that for LIB and SIB system, which might be due to the relatively larger radius of potassium ion.

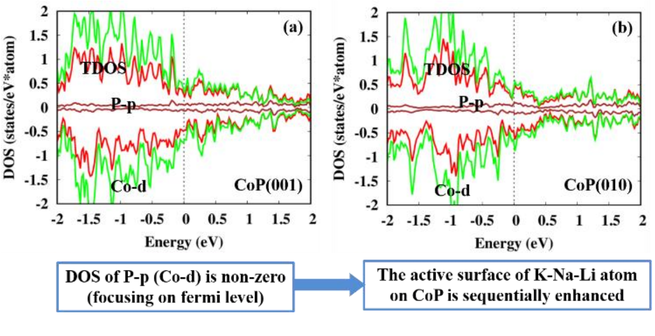

Figure 7. Density of states before and after Li, Na and K adsorption on the (a) CoP (001), and (b) (010) surfaces.

Based on the above results, it can be found that CoP@GF membrane exhibited much better cyclic ability and rate capability than CoP electrode in LIB, SIB and PIB systems. And the electrochemical properties of the electrode in alkali metal ion batteries can be ordered as LIBs > SIBs > PIBs. To shed light on the phenomenon, the density of states (DOS) before and after Li, Na and K adsorption on both of the CoP (010) and (001) surfaces were studied. The electrons around the Fermi level (Ef) played a significant role in the adsorption reactions. As shown in Fig. 7, it can be seen that the DOS at the Ef are all lower than the result obtained on the clean surfaces, indicating the electron transferred from the surface of CoP to Li, Na, and K.

Table 4. Calculated adsorption energy values of Li-CoP, Na-CoP, and K-CoP.

Surface	Adsorption element	Adsorption energy (eV)
CoP(001)	Li	-2.44
	Na	-1.58
	K	-1.38
CoP(010)	Li	-2.97
	Na	-2.30
	K	-2.26

For the DOS of the Li, Na and K adsorbed on the CoP (001) (Fig. 7a). It is calculated that the Li-CoP (001) exhibits the lowest adsorption energy with the value of -2.44 eV. While the Na-CoP (001) exhibits the adsorption energy with the value of -1.58 eV. However, the adsorption energy of K atom on the CoP (001) surface was calculated as -1.38 eV, demonstrating the K-CoP (001) shows the highest adsorption energy. For the DOS of the Li, Na and K adsorbed on the CoP (010) (Fig. 7b), It is calculated that the adsorption energy values were -2.97, -2.30, and -2.26 eV for Li-CoP (010), Na-CoP (010), and K-CoP (010), respectively, suggesting similar adsorption energy value order when compared to the result obtained on the CoP (001) (Table 4). The results indicate that more electrons at the CoP surfaces transfer to Li atom than Na and K, and the surface reactivity thus can be ordered as Li-CoP > Na-CoP > K-CoP. Thus, Li-CoP surface is the most active surface for the redox reaction. These calculated results demonstrate that the cobalt phosphide has better storage capacity for lithium than sodium and potassium, which is consistent with the experimental results.

Conclusion

CoP@GF hybrid membrane was synthesized by a facile phosphidation process and subsequent vacuum-filtrated method and utilized as a binder-free electrode for alkali metal (Li, Na, K) ion batteries. The synthesized CoP@GF exhibited enhanced energy storage properties in LIB, SIB, and PIB systems. It exhibited specific capacities of 832 mAh g^{-1} after 200 cycles in LIBs, 305 mAh g^{-1} after 200 cycles in SIBs, and 216 mAh g^{-1} after 100 cycles in PIBs, all of which are greatly outperforming that of CoP and GF membrane electrode. The electrochemical results indicated that the energy storage properties of CoP@GF electrodes in alkali metal ion batteries with an order of LIBs > SIBs > PIBs. The studies on adsorption energy of CoP surfaces for the Li, Na, and K through DFT method indicated that the surface reactivity can be ordered as Li-CoP > Na-CoP > K-CoP. That means higher electrochemical performance can be obtained in LIBs.

Experimental Section

Synthesis of Urchin-type CoP

Typically, 0.291 g $Co(NO_3)_2{\cdot}6H_2O$, 0.093 g NH_4F and 0.300 g urea were dissolved in 20 ml deionized water and stirred for 0.5 h, and then the solution was migrated into a Teflon-lined stainless autoclave (50 ml) and reacted at 120 °C for 6 h. After it, the solid precipitate of $2CoCO_3{\cdot}3Co(OH)_2{\cdot}H_2O$ was obtained through centrifugation and washed for six times with ethanol, and dried at 60 ºC for 12 h. To prepare CoP, NaH_2PO_2 and $2CoCO_3{\cdot}3Co(OH)_2{\cdot}H_2O$ were put at two separate locations in a railboat with the former at the upper reaches of the furnace. The molar ratio for P to Co is 5:1. Afterward, the samples were calcined at 300 °C for 180 min in a N_2 ambiance. After cooling down to ambient temperature, the CoP was acquired.

Synthesis of CoP@GF membrane

Typically, 0.020 g grapheme oxide and 0.020 g CoP were scattered in 10 ml deionized water by ultrasonication to form homogeneous suspension, which was then migrated into vacuum filtration and filtered via an organic millipore filter (0.22 µm of pore size). The composite membrane was kept on the millipore filter under sustained vacuum for another two hours before to fabricate a CoP@graphene oxide membrane. Finally, the CoP@graphene oxide membrane was calcined in an air ambiance at 200 °C for 2 h to obtain CoP@GF membrane. For comparison, the GF membrane was prepared using the same procedure without the introduction of CoP.

Details for Characterizations, Electrochemical tests and DFT calculation are presented in the Supporting Information.

Acknowledgements

This work is supported by the National Natural Science Foundation of China (No. 51972267, 51872226), the Scientific Research Fund of Shaanxi Provincial Education Department (No. 20JK0945), the Science & Technology Project Foundation of Xi’an (No. 2019KJWL09) and the National Training Program of Innovation and Entrepreneurship for Undergraduates (No. 201910697031).

Keywords: Cobalt phosphide • Graphene framworks • Hybrid membrane • Alkali metal ion batteries • Theoretical study

[1] D. Davies, M. Verde1, O. Mnyshenko, Y. Chen, R. Rajeev, Y. Meng, G. Elliott, *Nat. Energy* **2019**, *4*, 42-50.
[2] P. Zhang, F. Wang, M. Yu, X. Zhuang, X. Feng, *Chem. Soc. Rev.* **2018**, *47*, 7426-7451.
[3] T. Jin, Q. Han, L. Jiao, *Adv. Mater.* **2020**, *32*, 1806304.
[4] W. Zhang, Z. Yue, Q. Wang, X. Zeng, C. Fu, Q. Li, X. Li, L. Fang, L. Li, *Chem. Eng. J.* **2020**, *380*, 122548.
[5] R. Rajagopalan, Y. Tang, X. Ji, C. Jia, H. Wang, *Adv. Funct. Mater.* **2020**, *30*, 1909486.
[6] W. Zhang, P. Cao, Z. Zhang, Y. Zhao, Y. Zhang, L. Li, K. Yang, X. Li, L. Gu, *Chem. Eng. J.* **2019**, *364*, 123-131.
[7] X. Xiao, L. Zou, H. Pang, Q. Xu, *Chem. Soc. Rev.* **2020**, *49*, 301-331.
[8] K. Dinh, Q. Liang, C. Du, J. Zhao, A. Tok, H. Mao, Q. Yan, *Nano Today* **2019**, *25*, 99-121.
[9] G. Chang, Y. Zhao, L. Dong, D. Wilkinson, L. Zhang, Q. Shao, W. Yan, X. Sun, J. Zhang, *J. Mater. Chem. A* **2020**, *8*, 4996-5048.
[10] W. Miao, X. Zhao, R. Wang, Y. Liu, L. Li, Z. Zhang, W. Zhang, *J. Colloid Interface Sci.* **2019**, *556*, 432-440.
[11] K. Nam, Y. Hwa, C. Park, *ACS Appl. Mater. Interfaces* **2020**, *12*, 15053-15062.
[12] H. Gao, F. Yang, Y. Zheng, Q. Zhang, J. Hao, S. Zhang, H. Zheng, J. Chen, *ACS Appl. Mater. Interfaces* **2019**, *11*, 5373-5379.

[13] Y. Wu, H. Huang, Y. Feng, Z. Wu, Y. Yu, *Adv. Mater.* **2019**, *31*, 1901414.

[14] Y. Wang, Y. Lim, S. Huang, M. Ding, D. Kong, Y. Pei, T. Xu, Y. Shi, X. Li, H. Yang, *Nanoscale* **2020**, *12*, 4341-4351.

[15] K. Guo, B. Xi, R. Wei, H. Li, J. Feng, S. Xiong, *Adv. Energy Mater.* **2020**, *10*, 1902913.

[16] H. Li, S. Hao, Z. Tian, Z. Zhao, X. Wang, *Electrochim. Acta* **2019**, *321*, 134624.

[17] C. Jing, X. Song, K. Li, Y. Zhang, X. Liu, B. Dong, F. Dong, S. Zhao, H. Yao, Y. Zhang, *J. Mater. Chem. A* **2020**, *8*, 1697-1708.

[18] X. Yu, D. Tian, W. Li, B. He, Y. Zhang, Z. Chen, A. Lu, *Nano Res.* **2019**, *12*, 1193-1197.

[19] H. Yuan, M. Wu, J. Zheng, Z. Chen, W. Zhang, J. Luo, CB. Jin, O. Sheng, C. Liang, Y. Gan, *Adv. Funct. Mater.* **2019**, *29*, 1809051.

[20] B. Chen, D. Chao, E. Liu, M. Jaroniec, N. Zhao, S. Qiao, *Energy Environ. Sci.* **2020**, *13*, 1096-1131

[21] P. Ge, L. Zhang, W. Zhao, Y. Yang, W. Sun, X. Ji, *Adv. Funct. Mater.* **2020**, *30*, 1910599.

[22] X. Xu, J. Feng, J. Liu, F. Lv, R. Hu, F. Fang, L. Yang, L. Ouyang, M. Zhu, *Electrochim. Acta* **2019**, *312*, 224-233.

[23] J. Ni, X. Zhu, Y. Yuan, Z. Wang, Y. Li, L. Ma, A. Dai, M. Li, T. R. Shahbazian-Yassar, *Nat. Commun.* **2020**, *11*, 1212.

[24] T. Jin, Q. Han, L. Jiao, *Adv. Mater.* **2020**, *32*, 1806304.

[25] S. Jia, Y. Wang, X. Liu, S. Zhao, W. Zhao, Y. Huang, Z. Li, Z. Lin, *Nano Energy* **2019**, *59*, 229-236.

[26] W. Qiu, H. Xiao, Y. Li, X. Lu, Y. Tong, *Small* **2019**, *15*, 1901285.

[27] H. Guo, Q. Feng, K. Xu, J. Xu, J. Zhu, C. Zhang, T. Liu, *Adv. Funct. Mater.* **2019**, *29*, 1903660.

[28] W. Zhao, S. Ci, X. Hu, J. Chen, Z. Wen, *Nanoscale* **2019**, *11*, 4688-4695.

[29] G. Xia, J. Su, M. Li, P. Jiang, Y. Yang, Q. Chen, *J. Mater. Chem. A* **2017**, *5*, 10321-10327.

[30] Z. Liu, S. Yang, B. Sun, X. Chang, J. Zheng, X. Li, *Angew. Chem. Int. Ed.* **2018**, *130*, 10344-10348.

[31] J. Zhang, K. Zhang, J. Yang, G.H. Lee, J. Shin, V.W. Lau, Y.M. Kang, *Adv. Energy Mater.* **2018**, *8*, 1800283.

[32] E. Cao, Z. Chen, H. Wu, P. Yu, Y. Wang, F. Xiao, S. Chen, S. Du, Y. Xie, Y. Wu, Z. Ren, *Angew. Chem. Int. Ed.* **2020**, *59*, 4154-4160.

[33] J. Guo, B. Wang, D. Yang, Z. Wan, P. Yan, J. Tian, T. Isimjan, X. Yang, *Appl. Catal. Environ.* **2020**, *265*, 118584.

[34] B. Wang, Y. Xia, G. Wang, Y. Zhou, H. Wang, *Chem. Eng. J.* **2017**, *309*, 417-425.

[35] X. Li, B. Guan, S. Gao, X. Lou, *Energy Environ. Sci.* **2019**, *12*, 648-655.

[36] B. Wu, Y. Xie, Y. Meng, C. Qian, Y. Chen, A. Yuan, X. Guo, H. Yang, S. Wan, S. Lin, *J. Mater. Chem. A* **2019**, *7*, 6149-6160.

[37] Q. Chang, Y. Jin, M. Jia, Q. Yuan, C. Zhao, M. Jia, *J. Colloid Interface Sci.* **2020**, *575*, 61-68.

[38] Z. Zeng, C. Wei, C. Lu, Y. Shao, W. Guo, S. Dou, J. Sun, *Small* **2020**, *16*, 1906566.

[39] W. Miao, Y. Zhang, H. Li, Z. Zhang, L. Li, Z. Yu, W. Zhang, *J. Mater. Chem.* A **2019**, *7*, 5504-5512.

[40] W. Zhang, W. Miao, X. Liu, L. Li, Z. Yu, Q. Zhang, *J. Alloys Compd.* **2018**, *769*, 141-148.

Table of Contents

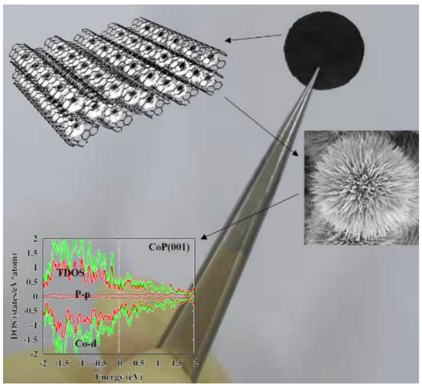

Urchin-type cobalt phosphide is encapsulated in graphene framework membrane as a binder-free electrode for alkali metal ion batteries. This membrane exhibits enhanced reversible lithium, sodium, and potassium storage capabilities. Moreover, the energy storage properties of the membrane electrodes are in the order of Li > Na > K, which is further studied by the adsorption energy of CoP surfaces for Li, Na, and K through DFT method.